

Thresholdless deep and vacuum ultraviolet Raman frequency conversion in hydrogen-filled photonic crystal fiber: supplementary material

MANOJ K. MRIDHA, DAVID NOVOA*, POORIA HOSSEINI, AND PHILIP ST.J. RUSSELL

Max Planck Institute for the Science of Light, Staudtstrasse 2, 91058 Erlangen, Germany

*Corresponding author: david.novoa@mpl.mpg.de

Published 28 May 2019

This document provides supplementary information to “Thresholdless deep and vacuum ultraviolet Raman frequency conversion in hydrogen-filled photonic crystal fiber,” <https://doi.org/10.1364/OPTICA.6.000731>. Here we give further details on the experimental set-up, fiber dispersion and the numerical simulations of the evolution of light pulses inside hydrogen-filled hollow-core photonic crystal fibers. In addition, we also discuss the spectral purity of the generated coherence waves, the influence of the pump energy on the UV conversion efficiency and the modeling of the UV performance of kagomé-type photonic crystal fibers.

1. Experimental set-up

Laser source.— We employed an injection-seeded Nd:YAG laser delivering 1064 nm, 3.2 ns pulses at 3 kHz repetition rate. As the inter-pulse separation of ~ 0.33 ms is much longer than the typical dephasing time of the Raman coherence (~ 1 ns), we can disregard any pulse-to-pulse effects. By frequency-doubling the laser pulses in a Potassium-Titanyl-Phosphate (KTP) crystal, we obtained the green pump source at 532 nm. The 266 nm mixing beam was then obtained by another frequency-doubling stage of the 532 nm pump in a Beta-Barium-Borate (BBO) crystal. An uncoated plano-convex CaF₂ lens with focal length 100 mm was used to launch both the pump and the mixing beam into the fiber. To mitigate the in-coupling mismatch of the two wavelengths due to chromatic aberration, we used two telescopes placed in the optical paths of both beams—before the dichroic mirror (see Fig. 2(a) in main text). The use of this arrangement resulted in independent control of the beam diameters of both beams, which facilitated their simultaneous coupling into the fiber.

Gas system.— The hollow-core photonic crystal fiber (HC-PCF) is placed in two 8-cm-long gas-cells connected by a hollow metallic tube. Light enters and exits the gas-cells through 3 mm thick and 10 mm in diameter MgF₂ optical windows. The pressure in the gas-cells was manually regulated with a very fine step size of ~ 50 mbar. This was made possible by the combined action of a number of gas-flow components: a coarse self-venting pressure regulator, a needle valve and a metering valve. The metering valve, when completely closed, played a key role in providing the minimum gas flow with additional control being provided by the needle valve.

2. Dispersion landscape of kagomé-type HC-PCF

The wavelength-dependent propagation constant $\beta_{ij}(\lambda)$ for the LP_{ij}-like modes of a gas-filled kagomé-style hollow-core photonic crystal fiber is analytically calculated using the modified Marcatili-Schmelzer model [1]

$$\beta_{ij}(\lambda) = k_0 \sqrt{n_{\text{gas}}^2(p, \lambda) - \lambda^2 u_{ij}^2 / (2\pi a)^2} \quad (\text{S1})$$

where u_{ij} is the j -th root of the i -th order Bessel function of the first kind, with (i, j) being also the azimuthal and radial mode orders, $k_0 = 2\pi / \lambda$ is the vacuum wavenumber, $n_{\text{gas}}(p, \lambda)$ is the pressure, p , and wavelength-dependent refractive index of the filling gas, and a is the area-preserving core radius. Note that this model disregards the influence of loss bands caused by anti-crossings between the core mode and modes in the glass walls surrounding the core, which are irrelevant in our experimental conditions as we have discussed in the main text.

3. Details of the numerical simulations

The evolution of the electric fields of the Raman sidebands, as well as the molecular coherence triggered by the green pump are modeled through a set of coupled Maxwell-Bloch equations involving several fiber modes [2]. As in the experiment, we considered a fiber length of 40 cm and core radius $a = 22$ μm . The material dispersion of hydrogen gas is adopted from [3]. Based on the experimental observations, only the fundamental, LP₀₁-like, and two-lobed or ring, LP₁₁-like, higher-order modes (HOM) were considered for the pump, mixing beam and their sidebands. To calculate the spatio-temporal evolution of the coherence waves in the system, we included three vibrational Stokes and anti-Stokes bands. For the green pump and its first Stokes band at 683 nm, we included measured loss values of 0.96 dB/m and 1.94 dB/m, respectively. Due to the lack of loss measurements for the

remaining Raman lines of the green pump and the mixing beam, their loss coefficients were free parameters, reasonably adjusted to get close agreement to the experiments (see Table S1–S2), although small variations of these values do not produce any significant changes in the observed dynamics.

Pump						
P_3	P_2	P_1	P_0	P_{-1}	P_{-2}	P_{-3}
4.34	2	2	0.96	1.94	30	20

Table S1. Numerical loss coefficients in dB/m for the different pump sidebands travelling in the fundamental mode.

Mixing						
M_3	M_2	M_1	M_0	M_{-1}	M_{-2}	M_{-3}
4	4	4	4	4	4	40

Table S2. Numerical loss coefficients in dB/m for the different mixing sidebands travelling in the fundamental mode.

For the two-lobed HOM, the losses of the different lines were simply double of those of the corresponding fundamental mode, an approximation that has been experimentally validated for similar fiber structures [4]. The mixing pulse was delayed by 1 ns with respect to the pump. The green pump was launched only in the fundamental mode. To obtain the numerical results shown in the main paper, we considered the initial injection of 100 nJ and 40 nJ of the mixing beam respectively in the fundamental and HOM mode. To model the initial stages of Raman amplification and subsequent ultraviolet scattering, a noise floor of 50 V/m was considered for all the Raman sidebands in both the modes, as well as for the pump in the HOM. Owing to the uncertainty in the measured Raman gain values at low pressures [5], the best agreement with the experiments involving 10 μ J of green pump energy launched in the fiber was obtained by considering 7 μ J of pump energy in the computations. Note that, for mixing pulse energies exceeding 1 μ J, our simplified numerical model for the dual-pump scheme is no longer valid as the back-action of the mixing beam on the generated molecular coherence cannot be disregarded.

4. Coherence wave generated mainly from the pump (532 nm) to Stokes (683 nm) transition

The beat-note created by two strong adjacent Raman sidebands is responsible for the excitation of coherence waves. In all the experimental spectra displayed in Fig. S1, the first vibrational Stokes (P_{-1}) is the strongest among all the vibrational Raman lines—only \sim 4 dB weaker than the pump. In addition, the rotational lines (separated by \sim 17.6 THz) are much weaker than the vibrational sidebands due to their lower gain, meaning that the generated coherence waves are mainly driven by the $P_0 - P_{-1}$ Raman transition. It is important to note that not only rotational SRS lines can influence the molecular coherence, but also higher-order vibrational Stokes sidebands can play a role. At low pressures, P_{-2} is more than 15 dB lower than P_{-1} even at high pump energies (see Fig. S1(a)-(b)). Figures S1(c-h) show the experimental output spectra recorded for two different pump energies at three different pressures of hydrogen. The number of Raman lines and their strength grows with increasing pressures and large pump energies—something expected as the Raman gain for hydrogen increases with pressure. Irrespective of the pressures shown, at relatively low pump energy of \sim 11 μ J, the P_{-2} signal is more than 30 dB weaker than the P_{-1} . However, for pump pulse energies of \sim 25 μ J, the P_{-2} signal grows significantly, and is less than 5 dB lower than the P_{-1} signal. In these conditions, the

coherence wave generated from $P_{-1} - P_{-2}$ transitions, although weaker, may influence the efficiency of the mixing beam depletion.

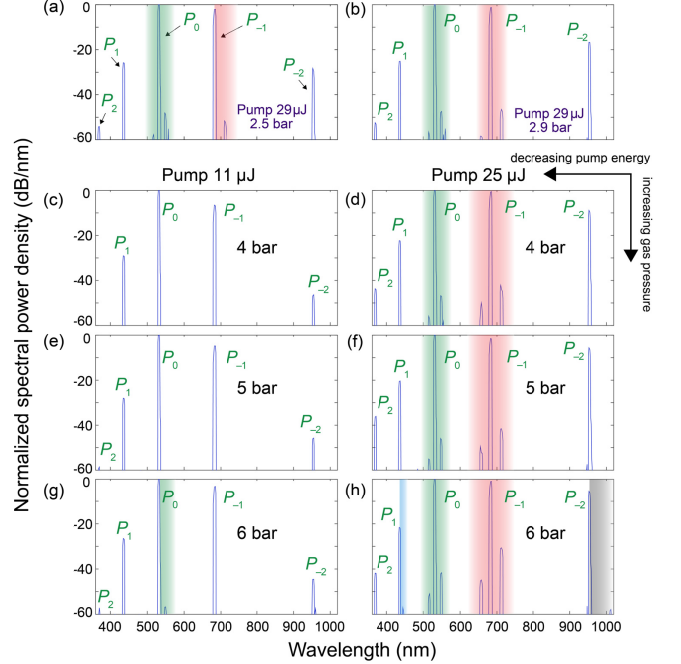


Fig. S1. (a) Spectra recorded at the output of the gas-filled HC-PCF for different gas pressures and launched pump energies. The spectra consist of a ro-vibrational Raman comb of the pump and the shaded regions enclose the rotational lines of the respective vibrational line or the pump. For each spectrum, all sidebands are normalized to the peak pump power.

5. Influence of the pump energy on the ultraviolet conversion efficiency

The complexity in the pressure-dependent conversion efficiency of the mixing beam increases with increasing pump pulse energy. This is verified experimentally in Fig. S2 and numerically in Fig. S3. Figure S2 displays the UV conversion efficiency for a launched green pump energy of \sim 18 μ J, larger than that employed in the experiments described in Fig. 3(a) in the main text. Comparing these two figures, there is a clear increase in complexity of the dynamics of the system as the gas pressure is varied.

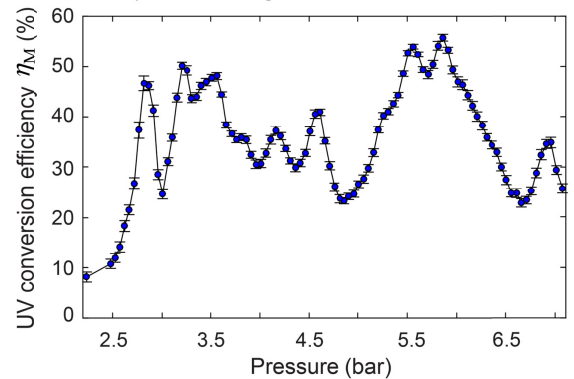


Fig. S2. Measured UV conversion efficiency for a launched green pump energy of \sim 18 μ J. The dynamics of the frequency conversion process becomes more complex for high pump energies (this is to be compared with the results shown in Fig. 3(a) of the main text).

Figure S3 plots the numerical results of the in-fiber dynamics of the mixing beam and the growth of its sidebands (M_2 to M_{-2}) for two different pump energies at two different pressures. In Fig. S3(a, b), the M_1 signal is the strongest among all the sidebands; the same occurs for M_{-2} in Fig. S3(c). This constitutes a further numerical

verification of the phase-matched generation process discussed in the main text and is also supported by Fig. S4. Irrespective of the pressure, it can be seen from these figures that upon increasing the pump energy, the generation of the sidebands reaches almost saturation in a relatively short fiber length. In addition, beyond this short distance within the fiber, all these lines oscillate and dynamically exchange energy over the remaining fiber length. These interactions make it difficult to accurately predict a priori the complex profile of the UV conversion efficiency recorded at the fiber output—as can be experimentally observed in Fig. S2.

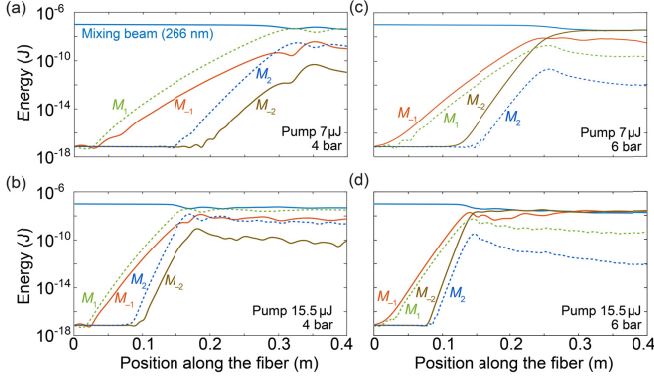


Fig. S3. (a) Simulated evolution of the fundamental mode content of the mixing beam and its higher-order Raman sidebands, ranging from M_2 to M_{-2} , along the fiber for two different gas pressures and pump energies. The launched energy of the mixing beam is 100 nJ. Individual lines follow the same color code throughout the four sub-figures.

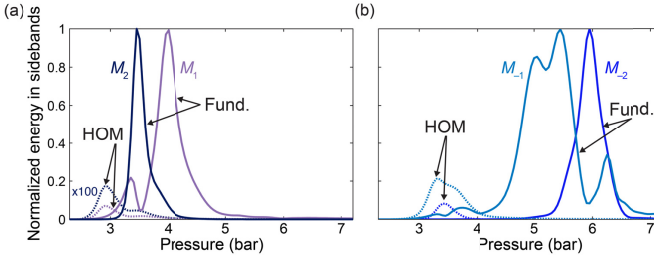


Fig. S4. (a) Simulated pressure-dependent generation of (a) M_1 (239 nm), M_2 (218 nm), (b) M_{-1} (299 nm) and M_{-2} (342 nm) for both fundamental and HOM mode contributions. The parameters used in the simulations are the same as in Fig. 3(a)-(b) in the main text. The energy of each individual Raman band is normalized to the peak of its respective fundamental mode content. The HOM mode content of the M_2 sideband is magnified by a factor of 100 for clarity. The pressure-dependent strengths of M_2 and M_{-2} reach their peaks around 3.5 bar and 6 bar, respectively, which correspond to the valleys displayed in the measurements of the M_1 and M_{-1} signals, as mentioned in the main text.

We also recorded the dependence of the measured pulse energy of the M_3 (199 nm) signal as a function of the green pump energy. At the optimum pump energy of ~ 20 μJ , more than 125 nJ of VUV light are generated (see Fig. S5).

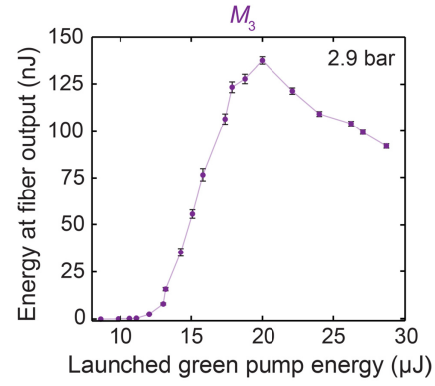


Fig. S5. Pulse energy of the M_3 (199 nm) signal measured at the fiber output for increasing launched green pump energies. This experimental energy scan was carried out for a DUV mixing pulse energy of 1.43 μJ and when filled with 2.9 bar of hydrogen.

6. Finite-element modeling of the UV performance of kagomé-PCF

We employed finite-element modeling to quantify the ultraviolet guidance of a canonical kagomé-PCF with the same structural parameters as that used in the experiments. As it can be seen in Fig. S6, all the spectral lines relevant to this work are nicely confined in the fiber core. Note that, although the M_2 signal at 218 nm lies close to the first-order anti-crossing at ~ 220 nm, only $\sim 1\%$ of the power is distributed outside the fiber core and hence the real part of its modal refractive index is not strongly affected.

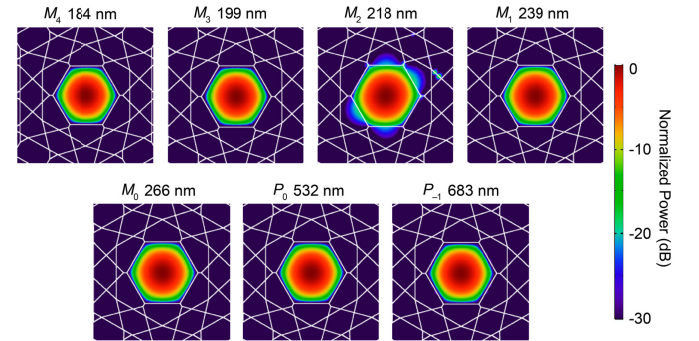


Fig. S6. Simulated power distribution of the fundamental mode for different ultraviolet wavelengths in a kagomé-style HC-PCF. The modes are calculated using finite-element modeling of a perfect kagomé-fiber structure with core-wall thickness of ~ 96 nm, flat-to-flat core-wall diameter of 22 μm and silica glass as the fiber material.

References

1. M. A. Finger, N. Y. Joly, T. Weiss, and P. St.J. Russell, "Accuracy of the capillary approximation for gas-filled kagomé-style photonic crystal fibers," Opt. Lett. **39**, 821 (2014).
2. S. T. Bauerschmidt, D. Novoa, A. Abdolvand and P. St.J. Russell, "Broadband-tunable LP_{01} -mode frequency shifting by Raman coherence waves in a H_2 -filled hollow-core photonic crystal fiber," Optica **2**, 536 (2015).
3. E. R. Peck and S. Huang, "Refractivity and dispersion of hydrogen in the visible and near infrared", J. Opt. Soc. Am. **67**, 1550 (1977).
4. B. M. Trabold, D. Novoa, A. Abdolvand, and P. St.J. Russell, "Selective excitation of higher order modes in hollow-core PCF via prism coupling", Opt. Lett. **39**, 3736 (2014).
5. W. K. Bischel and M. J. Dyer, "Wavelength dependence of the absolute gain coefficient for the $Q(1)$ transition in H_2 ", J. Opt. Soc. Am. B **3**, 677 (1986).